

Probing the Growth of Massive Black Holes with Black Hole-Host Galaxy Spin Correlations

ZHEN PAN¹ AND HUAN YANG^{1,2}

¹*Perimeter Institute for Theoretical Physics, Waterloo, Ontario N2L 2Y5, Canada*

²*University of Guelph, Guelph, Ontario N2L 3G1, Canada*

Submitted to ApJ

ABSTRACT

Supermassive black holes (SMBHs) are commonly found at the centers of their host galaxies, but their formation still remains an open question. In light of the tight correlation between the black hole (BH) mass and the velocity dispersions of the bulge component of the host galaxy, a BH-host galaxy coevolution scenario has been established. Such description however still contains many theoretical uncertainties, including the puzzles about the formation of BH seeds at high redshifts and the growth channel fueling these seeds. In this work, we systematically analyze the signatures of different growth channels on massive BH (MBH) spins. We show that different growth channels can be partially distinguished with the magnitudes of MBH spins inferred from extreme-mass-ratio-inspirals detected by the Laser Interferometer Space Antenna. In addition, we propose to measure the correlation between the directions of MBH spins and their host galaxy spins, which is possible for extreme mass-ratio inspirals happening in low-redshift galaxies ($z \leq 0.3$). With the inclusion of spin direction correlation different formation channels shall be significantly better constrained.

Keywords: Gravitational waves (678); Supermassive black holes (1663); Galaxy mergers(608)

1. INTRODUCTION

Supermassive black holes (SMBHs) are commonly found at the centers of their host galaxies. Empirical correlations have also been extensively explored (Ferrarese & Merritt 2000; McConnell & Ma 2013; Kormendy & Ho 2013) between the black hole (BH) masses, M , and different properties of their host galaxies, including the velocity dispersion σ_* of bulge stars in the host galaxies. The tight $M - \sigma_*$ relation in combination with other correlations has inspired an interpretation that BHs and their host galaxies coevolve by regulating each other's growth (Marconi & Hunt 2003; Kormendy & Ho 2013). The coevolution scenario provides a framework that connects the galaxy evolution with BH activities. However, there are still many important questions that this coevolution scenario provides no definitive answers, especially the ones related to the SMBH formation, including the formation of BH seeds and the growth channels fueling these seeds.

BH seeds can be general classified as light seeds with masses in the range of $\sim (10^2, 10^3)M_\odot$ and heavy seeds within the range of $\sim (10^4, 10^6)M_\odot$ (see e.g., Rees 1984; Latif & Ferrara 2016; Haemmerlé et al. 2020, for reviews). The light seeds are thought as results of collapse of metal-free population III stars (Madau & Rees 2001; Omukai 2001; Abel et al. 2002; Heger & Woosley 2002) and the heavy seeds are proposed to come from direct collapse of a massive protogalactic gas cloud (Begelman et al. 2006; Mayer et al. 2010; Di Matteo et al. 2012) or efficient merging stellar-mass compact objects in a gas-rich environment (Boco et al. 2020). Recently, Fragione & Silk (2020) proposed that repeated mergers of stellar mass BHs in nuclear star clusters can produce both light and heavy seeds depending on the cluster masses and densities. Starting from the seeds at high redshifts, BHs further accumulate masses by either merging with other BHs or accreting gas, both of which seem to be compatible with available observations, including the $M - \sigma_*$ relation (King 2003; Volonteri et al. 2003; Marconi et al. 2004; Volonteri & Rees 2005; King & Pringle 2006; Murray et al. 2005; Peng 2007). As shown by Sesana et al. (2009) and Sesana et al. (2011), both the seed formation and the BH growth history leave imprints on the mass function of massive BH (MBH)

zpan@perimeterinstitute.ca

hyang@perimeterinstitute.ca

binaries¹, which can be probed from the LISA detection of MBH coalescence from redshift $z = 10 \sim 15$ to local universe (Hughes 2002; Barausse et al. 2015; Amaro-Seoane et al. 2017).

Besides mass distributions, it is also natural to expect different models of seed formation and BH growth will also lead to different signatures on MBH spins, as discussed in (Berti & Volonteri 2008). MBH spins (both magnitudes and directions) can be accurately measured by LISA from extreme-mass-ratio-inspiral (EMRI) events (Huerta & Gair 2009; Gair et al. 2017; Babak et al. 2017), with the spin magnitudes expected to be measured with fractional uncertainty $\sim (10^{-6}, 10^{-4})$ and the spin directions expected to be constrained within $\sim (10^{-1}, 10^2)$ degree², which enables an accurate spin distribution reconstruction. In this work, we propose to include another observable - the correlation between the spin directions of MBHs and their host galaxies, to further sharpen our ability to distinguish different formation models. Such observable relies on the host galaxy identification, which is possible for several percents of the EMRI events, and galaxy spectroscopic surveys (Bundy et al. 2015) to determine the galaxy spin orientation.² We systematically analyze the spin signatures of different growth channels assuming the natural light seeds scenario, and explore how likely it is to distinguish various channels with the spin information of MBHs using a Bayes method.³ In particular, for the first time we include the MBH-host galaxy spin correlations in the analysis, which turns out to be a powerful probe to these growth channels.

The structure of the paper is organized as follows. In Section 2, we outline the growth channels and model their signatures on MBH spins and on the BH-host galaxy spin direction correlations. In Section 3, we introduce how well the MBH spins can be extracted from the EMRI waveforms and how many host galaxies of EMRIs can be identified in the LISA mission. In Section 4, we show how to distinguish different growth models from the spin information using the method

¹ We call BHs with masses $\sim (10^5, 10^7)M_\odot$ as MBHs.

² Galaxy spin orientations inferred from spectroscopic surveys have been used to probe the initial conditions in the early universe (Motloch et al. 2020).

³ MBHs stemming from light seeds accumulated almost all their masses via growth and their spins are completely determined by their growth history. However, MBHs stemming from heavy seeds accumulated less masses from growth or did not grow at all, therefore their spins depend more on the initial condition, i.e., the seed formation mechanism, which is vaguely understood now but can be probed by high-redshift MBH mergers that are expected to be detected by LISA (Amaro-Seoane et al. 2017), Einstein Telescope (Maggiore et al. 2020) and DECIGO (Kawamura et al. 2020). The method of distinguishing different growth channels described in this paper equally applies to the heavy seed scenario, as long as the seed formation mechanism is understood.

of Bayesian model selection. Some final remarks are given in Section 5.

In this paper, we assume a flat Λ CDM cosmology with $\Omega_m = 0.3$ and $H_0 = 70$ km/s/Mpc, and we use geometrical units $G = c = 1$.

2. GROWTH MECHANISMS OF MBHS AND THEIR IMPACTS ON BH SPINS

In this section, we review different growth channels of MBHs and obtain their corresponding implication on MBH spins, including the magnitude distribution of MBH spins and the MBH spin- galaxy spin correlation.

2.1. Accretion

Coherent Accretion. Accretion can be an efficient channel for MBHs to gain their masses (Kawaguchi 2003; Kawaguchi et al. 2004; King & Pringle 2006; Li 2012). If a central BH is spun up with the large-scale gas fueling in a disk like configuration, the accretion is coherent. In the standard thin-disk accretion, the BH could be spun up to a maximum value $a = 0.998$ limited by the preferential accretion of low-angular-momentum photons (Thorne 1974). In a magnetized disk, the equilibrium spin is $a \sim 0.95$ (Gammie et al. 2004; Shapiro 2005). In this work, we do not intend to distinguish the subtle differences arising from various assumptions on accretion physics, and we choose to describe the spin magnitudes of MBHs with a coarse probability distribution $|a| \sim \mathcal{N}(1, 0.05)$, where $\mathcal{N}(\mu, \sigma)$ is a normal distribution with a mean value μ and a standard deviation σ (here we use $\sigma = 0.05$ to take account of typical variation of equilibrium BH spin magnitudes assuming different accretion physics). Following coherent accretion, the BH spin up to nearly extremal state, with its spin direction nearly aligned with the rotation direction of the accretion disk. The initial spin magnitude and direction are no longer relevant after the BH mass increases by one or more e-folds. As a result, the BH spin direction \hat{a} should be aligned with the rotation direction \hat{L} of the large-scale gas disk. In reality, the gas disk may be turbulent and sometimes clumpy with its local rotation direction slightly off its mean value (see e.g., Souza Lima et al. 2017). Though this variation is hard to calculate from first principle, we may perform a rough estimate based on two quantities: the aspect ratio of the accretion disk $h := H/r$ and the inclination angle $\iota_{\text{gas,star}}$ between the gas disk and the stellar disk in the same galaxy. In the classical Mestel model of the gas disk (Mestel 1963), h is in the range of $\sim (0.05, 0.1)$. The inclination angles $\iota_{\text{gas,star}}$ are measured from galaxy spectroscopic surveys to be $\sim 10^\circ$ (Krolewski et al. 2019). Therefore, we take $\delta\hat{L} \approx 10^\circ$ as a reference and use an ansatz that $\cos^{-1}(\hat{a} \cdot \hat{L}) \sim \mathcal{N}(0, 10^\circ)$ in the following discussion.

Chaotic Accretion. The accretion is ‘chaotic’ if it consists of many short chaotic episodes with different accretion direc-

tion in each one. In this case, the distribution of BH spins is mainly determined by $\Delta M/M$, the fractional BH mass increase in each episode. If $\Delta M/M \gtrsim 1$, The disk angular momentum in each episode is large enough to drive the BH to high spin no matter what the initial spin is; while in episodes with $\Delta M/M \ll 1$ BH tends to spin down, because the BH mass increases linearly with the number of accretion episodes N_{acc} while the angular momentum gain is proportional $\sqrt{N_{\text{acc}}}$ due to the random-walk cancellation (King & Pringle 2006; King et al. 2008; Wang et al. 2009; Dotti et al. 2013; Volonteri et al. 2013; Li & Cao 2019; Zhang & Lu 2019).

In the beginning of each accretion episode, the BH spin is in general misaligned with the disk angular momentum, and the inner part of the disk will be wrapped in a viscous timescale (known as the Bardeen-Petterson effect (Bardeen & Petterson 1975)). The wrapped disk will exert a torque onto the central BH and align or anti-align the BH spin with the angular momentum of the outer disk in a timescale (Scheuer & Feiler 1996; Natarajan & Pringle 1998; King et al. 2005; Lodato & Gerosa 2013; Gerosa et al. 2020) $t_{\text{align}} \sim (M/\dot{M})\alpha^{5/3}a^{2/3}h^{2/3}$ assuming a standard α -disk description (Shakura & Sunyaev 1973), where \dot{M} is the accretion rate and $h = H/r$ is the aspect ratio of the disk. After the alignment, the central BH will be spun up as accreting the gas. Together with the accretion timescale $t_{\text{acc}} = \Delta M/\dot{M}$, we obtain

$$\frac{t_{\text{align}}}{t_{\text{acc}}} \simeq \frac{5 \times 10^{-3}|a|^{2/3}}{\Delta M/M} \left(\frac{\alpha}{0.1}\right)^{5/3} \left(\frac{h}{0.1}\right)^{2/3}. \quad (1)$$

Therefore, we can safely ignore the short alignment period in calculating the final BH spin of each accretion episode as long as $\Delta M/M \gg 5 \times 10^{-3}|a|^{2/3}$.

In each accretion episode, the BH angular momentum J changes with its mass M as

$$dJ = l(a)M dM_{\text{gas}} = \frac{l(a)}{e(a)} M dM, \quad (2)$$

where $J = aM^2$, with a being the dimensionless spin which is negative if the BH spin is anti-aligned with the angular momentum of the accretion disk; $l(a)$ and $e(a)$ are the specific angular momentum and specific energy of particles on the innermost stable circular orbit (ISCO) $r_{\text{isco}}(a)$ with the following explicit forms (Bardeen et al. 1972)

$$e(a) = \frac{r_{\text{isco}}^{3/2} - 2r_{\text{isco}}^{1/2} + a}{r_{\text{isco}}^{3/4} (r_{\text{isco}}^{3/2} - 3r_{\text{isco}}^{1/2} + 2a)}, \quad (3)$$

$$l(a) = \frac{r_{\text{isco}}^2 - 2ar_{\text{isco}}^{1/2} + a^2}{r_{\text{isco}}^{3/4} (r_{\text{isco}}^{3/2} - 3r_{\text{isco}}^{1/2} + 2a)};$$

dM_{gas} is the mass element of accreted gas, a fraction $1 - e(a)$ of which is converted to radiation escaping to infinity and the

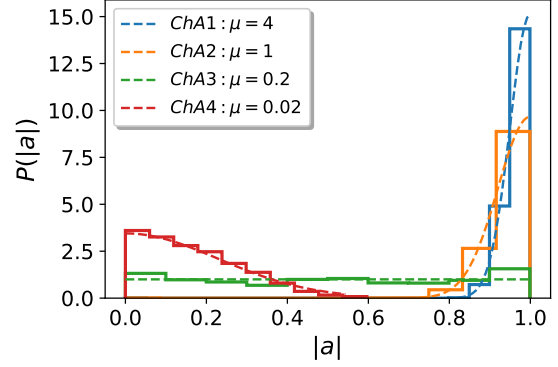


Figure 1. Distribution of BH spins driven by chaotic accretion with fractional mass increase $\Delta M/M \sim \mathcal{N}(\mu, \sigma)$ in each accretion episode, where solid lines are the simulation results and the dashed lines are the corresponding Gaussian fits. Here we take $\sigma = 0.1\mu$ as an example, and larger σ , say, $\sigma = 0.2\mu$ only slightly broadens $P_{|\mu=1}$ and makes little change to remaining 3 distributions.

remaining fraction $e(a)$ is absorbed by the BH. As a result, we obtain the following simple evolution equation

$$da = \left[\frac{l(a)}{e(a)} - 2a \right] d \ln M, \quad (4)$$

where the specific angular momentum in retrograde accretion is larger than in direct accretion $l(a < 0) > l(a > 0)$, leading to a larger spin magnitude change in retrograde accretion than in direct accretion for a same mass increase $\Delta(\ln M)$.

We consider a simple chaotic accretion model: in the beginning of each episode (after the short alignment process), the BH spin is assumed to be aligned or anti-aligned with the angular momentum of the accretion disk with equal chance and the BH increases by $\Delta M/M \sim \mathcal{N}(\mu, 0.1\mu)$. To take account of the equilibrium BH spin as in the coherent accretion case, we enforce a spin distribution $P(a) \propto \mathcal{N}(1, 0.05)$ for $a > 0.9$. In Fig. 1, we show four example models of chaotic accretion (ChA1, ChA2, ChA3, ChA4 with $\mu = 4, 1, 0.2, 0.02$ respectively), where the spin distribution $P(|a|)$ is same to that of coherent accretion for $\mu \gtrsim 1$ because the angular momentum gain is large enough to drive the BH to high spin whatever the initial spin is, and $P(|a|)$ peaks on zero for $\mu \ll 1$. In the case of $\mu \ll 1$, the BH will be spun up ($|a| \uparrow$) in direct accretion ($a > 0$) and will be spun down ($|a| \downarrow$) in retrograde accretion ($a < 0$). As the spinning down is more efficient than the spinning up (see the explanation following Eq. (4)), the net result is an equilibrium distribution $P(|a|)$ that peaks on $a = 0$ and decreases with $|a|$. In the case of chaotic accretion, we expect no BH-host galaxy spin direction correlation, i.e., $\hat{a} \cdot \hat{L} \sim \mathcal{U}(-1, 1)$, where \mathcal{U} is a uniform distribution.

2.2. Mergers

Dry Mergers. MBH may merge following the merger of their host galaxies. This is considered as a natural growth

channel for MBHs considering galaxies commonly harbor MBHs. These mergers can be further classified as wet mergers (mergers in a gas-rich environment) and dry mergers (mergers in a gas-poor environment) (see e.g., Colpi 2014, for a review). For dry mergers there are three main phases along the path to the final coalescence (Begelman et al. 1980): (i) an early phase of pairing when MBHs migrate inwards driven by the dynamical friction with background stars, until the two MBHs form a Keplerian binary (Chandrasekhar 1943; Begelman et al. 1980); (ii) a binary hardening phase when the binary separation decreases by ejecting stars of close encounters (Yu 2002; Milosavljević & Merritt 2003); (iii) a gravitational inspiral phase when the binary orbital decay is driven by the emission of GWs until the final coalescence. For mergers of nearly equal mass BHs, the spins of remnant BHs peak around $a \simeq 0.69$, while mergers of small mass ratio BHs tend to produce remnant BHs with larger spin dispersion (Barausse & Rezzolla 2009). In the dry mergers of binary BHs, there is no apparent mechanism that aligns the BH spin directions \hat{a}_1, \hat{a}_2 with their orbital direction \hat{L}_{12} or aligns the orbital direction \hat{L}_{12} with the host galaxy spin direction \hat{L} , i.e., \hat{a}_1, \hat{a}_2 and L_{12} are randomly oriented. Berti & Volonteri (2008) investigated the cosmological spin evolution of BHs driven by dry mergers (or isotropy mergers in their language) and they found the distribution of MBH spins peaks around ~ 0.7 with a long tail extending to small spins (we fit their histogram of BH spins with a skewed Gaussian distribution and plot in Fig. 2). The spin direction of the remnant BH should also be randomly oriented with respect to the spin direction of the host galaxy, i.e., $\hat{a} \cdot \hat{L} \sim \mathcal{U}(-1, 1)$.

Wet Mergers. If the two merging galaxies are gas rich, a stellar disk and a gas disk form in the remnant galaxy, so that the two MBHs undergo roughly four different phases before the final coalescence (Mayer et al. 2007): (i) an early pairing phase when MBHs wander beyond the scope of the gas disk and migrate inwards due to the dynamical friction with background stars; (ii) a pairing phase when the motion of MBHs is influenced by the gravity of the gas disk (called circumnuclear disk) and migrate inwards driven by the torque from the density-wave excitations in the disk (similar to the Type I planet migration) (Dotti et al. 2006, 2007; Mayer et al. 2007; Colpi et al. 2009; Mayer 2013); (iii) a hardening phase when the two MBHs form a Keplerian binary surrounded by a circum-binary disk and migrate under the binary-disk coupling arising from two opposing actions that the binary tidal fields open gaps in the disk whereas viscous torque fills the gaps (similar to the Type II planet migration) (Armitage & Natarajan 2002; Armitage 2013); (iv) and an inspiral phase dominated by GW emission.

As a MBH with mass M ram into the disk with an inclination angle ι , the inclination angle will be damped by the

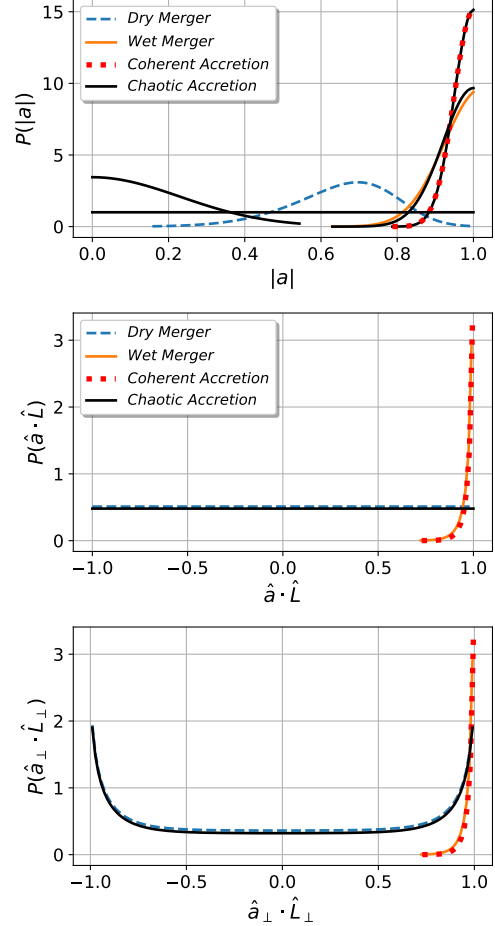


Figure 2. Upper panel: probability distribution functions of MBH spins of different growth channels, where we show four chaotic accretion models with BH mass increase fraction $\Delta M/M \simeq 4, 1, 0.2, 0.02$ in each accretion episode, respectively (also see Fig. 1). Middle panel: distributions of MBH-host galaxy spin direction correlations $\hat{a} \cdot \hat{L}$. Lower panel: distributions of projected correlations $\hat{a}_\perp \cdot \hat{L}_\perp$, where \perp marks the projection to the plane perpendicular to the LoS.

BH-disk interaction. Now we are to calculate the timescale of this process. Assuming the disk volume density, surface density, circular velocity and sound speed at radius r are $\rho(r)$, $\Sigma(r)$, $V_d(r)$ and $c_s(r)$, respectively. The disk aspect ratio h is approximately $h \simeq c_s/V_d$ and we take $h = 0.1$ as a fiducial value. Gas bounded by the BH within radius $r_b = GM/V_d^2$ will be shocked and accelerated to roughly the same velocity of the BH. In a self-gravitating circum-nuclear disk, the BH speed is approximately V_d . Therefore the disk-BH interacting force is roughly $F = \dot{m}_{\text{gas,ac1}} V_d = \rho \pi r_b^2 V_d^2$ with $\dot{m}_{\text{gas,ac1}}$ being the amount of shocked and accelerated gas per unit time and the inclination damping timescale is

$$t_{\text{damp}} = \frac{MV_d \sin \iota \pi \sin \iota}{F_\perp h} = \frac{M}{(GM/V_d^2)^2 \Sigma(r)} \frac{r \sin \iota}{V_d}, \quad (5)$$

where $F_{\perp} = F \sin \iota$ is the component perpendicular to the disk and factor $\pi \sin \iota / h$ takes account of the fact that only a fraction of the BH orbit is inside the disk for $\iota > h$. We consider a Mestel model of the circum-nuclear disk (Mestel 1963; Escala et al. 2005). The disk is self-gravitating and axisymmetric, with a constant rotational velocity V_d , which is related to the total disk mass M_d and the disk size R_d by $V_d = \sqrt{GM_d/R_d}$. The gas mass within radius r is $M_{\text{gas}}(r) = M_d r/R_d$ and disk surface density at each radius is $\Sigma(r) = M_d/(2\pi R_d r)$. Using these relations, we find

$$t_{\text{damp}} = \frac{M_{\text{gas}}(r)}{M} \frac{2\pi r}{V_d} \sin \iota$$

$$\stackrel{r=r_T}{\sim} 5 \text{ kyr} \times \sin \iota \left(\frac{r_T}{0.1 \text{ pc}} \right) \left(\frac{V_d}{100 \text{ km/s}} \right)^{-1}, \quad (6)$$

where r_T is where $M_{\text{gas}}(r) = M$, i.e., the transition radius from the circum-nuclear disk phase to the circum-binary disk phase. The timescale of inclination damping is much shorter than the typical migration timescale, so we expect the gas disk and the binary BH orbit are coplanar at the end of the circum-nuclear disk phase, $\hat{\mathbf{L}}_{12} \cdot \hat{\mathbf{L}} \approx 1$.

In the circum-binary disk phase, the inner part of the disk will be warped if the BH spin $\hat{\mathbf{a}}_{1,2}$ and the rotation direction of the disk $\hat{\mathbf{L}}$ are misaligned. It is still not clear whether the interaction between the BH binary and the warped disk can efficiently align them, though a number of studies have been performed previously (see e.g., Dotti et al. 2010; Maio et al. 2013; Lodato & Gerosa 2013; Gerosa et al. 2020). However, as shown by Barausse & Rezzolla (2009) and Hofmann et al. (2016), the spin direction of the remnant BH $\hat{\mathbf{a}}$ produced in the final coalescence is roughly aligned with the direction of the total angular momentum of the binary BH system at the beginning of the gravitational inspiral phase to high precision with $\cos^{-1}(\hat{\mathbf{a}} \cdot \hat{\mathbf{J}}_{\text{ini}}) \sim \mathcal{N}(0, 5^\circ)$. Here \mathbf{J}_{ini} is the initial total angular momentum dominated by the orbital angular momentum \mathbf{L}_{12} at large separations, and \mathbf{L}_{12} aligns with the spin direction of the gas disk \mathbf{L} as shown above. In combination with the intrinsic $\sim 10^\circ$ variation in the gas disk direction $\hat{\mathbf{L}}$ (see section 2.1), we obtain $\cos^{-1}(\hat{\mathbf{a}} \cdot \hat{\mathbf{L}}) \sim \mathcal{N}(0, \sqrt{(5^\circ)^2 + (10^\circ)^2})$. Berti & Volonteri (2008) also simulated the spin magnitudes of MBHs from aligned mergers and we again fit the histogram they obtained with a skewed Gaussian distribution (Fig. 2).

At this point, we have outlined the basic pictures of the different growth channels of MBHs. The corresponding BH spin distribution $P(|a|)$ and the BH-host galaxy spin direction correlations $\hat{\mathbf{a}} \cdot \hat{\mathbf{L}}$ are also derived respectively. However, $\hat{\mathbf{a}} \cdot \hat{\mathbf{L}}$ is not an ideal observable, because the 3D galaxy spin direction $\hat{\mathbf{L}}$ is not easy to measure, whereas its 2D projection $\hat{\mathbf{L}}_{\perp}$ onto the plane perpendicular to the line of sight (LoS) can be accurately measured to $\approx 1^\circ$ precision in galaxy spectroscopic surveys (e.g., MaNGA, Bundy et al. (2015);

Krolewski et al. (2019)). Therefore, we also need to calculate the probability distributions of 2D spin direction correlation $\hat{\mathbf{a}}_{\perp} \cdot \hat{\mathbf{L}}_{\perp}$. For a given distribution $P(\hat{\mathbf{a}} \cdot \hat{\mathbf{L}})$, we sample 32 data $\hat{\mathbf{a}} \cdot \hat{\mathbf{L}}$ points in concordance with the probability distribution; and for each pair of $\hat{\mathbf{a}}, \hat{\mathbf{L}}$, we uniformly sample 1024 directions of LoS, project the 3D directions $\hat{\mathbf{a}}, \hat{\mathbf{L}}$ onto the plane perpendicular to the LoS and calculate the 2D correlation $\hat{\mathbf{a}}_{\perp} \cdot \hat{\mathbf{L}}_{\perp}$. We finally obtain a histogram of all $\hat{\mathbf{a}}_{\perp} \cdot \hat{\mathbf{L}}_{\perp}$ data points and fit it with a smooth distribution function $P(\hat{\mathbf{a}}_{\perp} \cdot \hat{\mathbf{L}}_{\perp})$ (Fig. 2). We find $P(\hat{\mathbf{a}}_{\perp} \cdot \hat{\mathbf{L}}_{\perp}) \approx P(\hat{\mathbf{a}} \cdot \hat{\mathbf{L}})$ for Wet Merger and Coherent Accretion, and $P(\hat{\mathbf{a}}_{\perp} \cdot \hat{\mathbf{L}}_{\perp})$ peaks on ± 1 for Dry Merger and Chaotic Accretion with uniform $P(\hat{\mathbf{a}} \cdot \hat{\mathbf{L}})$ due to projection distortion, i.e., there is a large chance of projecting $\hat{\mathbf{a}} \cdot \hat{\mathbf{L}} \approx 0$ to $\hat{\mathbf{a}}_{\perp} \cdot \hat{\mathbf{L}}_{\perp} \approx \pm 1$, while the chance of projecting $\hat{\mathbf{a}} \cdot \hat{\mathbf{L}} \approx \pm 1$ to $\hat{\mathbf{a}}_{\perp} \cdot \hat{\mathbf{L}}_{\perp} \approx 0$ is small.

3. LISA DETECTION OF EMRIS AND HOST GALAXIES IDENTIFICATION

The expected EMRI rate depends on the mass function of MBH population at different redshifts, the fraction of MBHs living in dense stellar cusps where stellar-mass BHs are produced, EMRI rate per MBH and properties of stellar-mass BHs in the cusps. Babak et al. (2017) quantified each of these astrophysical ingredients with semi-analytical models and calculated the corresponding expected EMRI rates. They found tens to thousands of EMRIs per year should be detectable by LISA taking into account astrophysical uncertainties. In particular, ~ 6 to ~ 180 low-redshift ($z \leq 0.5$) EMRIs are expected to be detected by LISA per year for the majority of the models considered (Gair et al. 2017). For all detectable EMRIs, the typical fractional errors of intrinsic parameters, e.g., red-shifted masses and MBH spins, are found in the range of $(10^{-6}, 10^{-4})$ (Babak et al. 2017). Luminosity distance can be constrained with precision $\sigma(\ln D_L) \approx \rho^{-1}$ and the median sky resolution is approximately $\sigma(\Omega_s) \approx 0.05(\rho/100)^{-5/2}$ degree², where ρ is the signal to noise ratio (SNR) of the EMRI event (McGee et al. 2020).

Based on these results, we expect there is a fraction of low-redshift EMRIs that can be localized to small 3D error boxes containing a single galaxy. Therefore the host galaxies of these EMRIs can be identified from the corresponding LISA observation. Following the approach in (Babak et al. 2017), we consider a power-law mass function of the EMRI population with a redshift-independent EMRI rate R_0 at redshift $z \leq 0.5$,

$$\frac{dR_0}{d \ln M} \propto M^{\alpha} \quad (\text{for } 10^5 M_{\odot} < M < 10^6 M_{\odot}) \quad (7)$$

with power index $\alpha = -0.5$ or 0 . At each redshift z , we sample 128 EMRIs with the MBH mass sampled from Eq. (7), the MBH spin chosen as $a = 0.98$, the companion BH mass set to be $m = 10M_{\odot}$, the binary orbital eccentricity at plunge

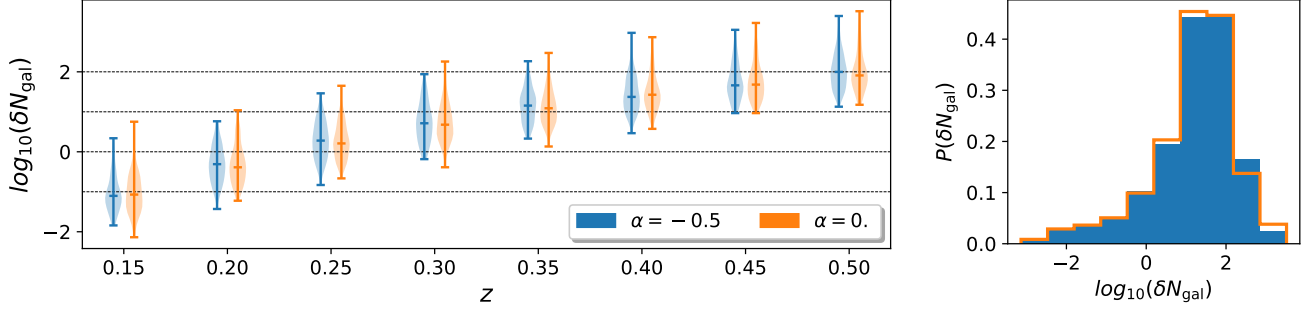


Figure 3. Left panel shows the distribution of expected number of galaxies δN_{gal} in each error box of the LISA detected EMRIs. Right panel shows the histogram of $\log_{10}(\delta N_{\text{gal}})$ for all detected EMRIs with redshift $z < 0.5$, where $P(\delta N_{\text{gal}} \leq 1) = 13\%$, $P(1 < \delta N_{\text{gal}} \leq 10) = 21\%$ and $P(10 < \delta N_{\text{gal}} \leq 100) = 48\%$ for mass function with power index with $\alpha = -0.5$, and the histogram for mass function with $\alpha = 0$ is approximately the same.

being $e_p = 0.1$, the luminosity distance $D_L(z)$, and 8 randomly sampled angles (including the source sky localization angles (θ_s, ϕ_s) and the MBH spin direction angles (θ_a, ϕ_a)) that uniquely determine the binary configuration at coalescence (see Chua & Gair (2015); Chua et al. (2017) for details). For each EMRI, we model its GWs with the Augment Analytic Kludge (AAK) waveform (Chua et al. (2017)) and record the time-domain waveforms $h_I(t)$ and $h_{II}(t)$ in the last two years before coalescence (I and II mark the two orthogonal LISA channels), where (Barack & Cutler 2004; Rubbo et al. 2004)

$$\begin{aligned} h_I(t) &= h_+(t)F_I^+(t) + h_\times(t)F_I^\times(t), \\ h_{II}(t) &= h_+(t)F_{II}^+(t) + h_\times(t)F_{II}^\times(t), \end{aligned} \quad (8)$$

with $h_{+,\times}$ being the waveforms of two polarizations and $F_{I,II}^{+,\times}$ are the corresponding detector antenna patterns of the two channels.

The SNR of EMRI GWs is calculated as $\rho = \sqrt{\langle h_I|h_I \rangle + \langle h_{II}|h_{II} \rangle}$ with the inner product defined as

$$\langle u|v \rangle := 4 \int_0^\infty \frac{\mathcal{R}[u(f)v^*(f)]}{P_n(f)} df, \quad (9)$$

where \mathcal{R} denotes the real part and $P_n(f)$ is the combination of one-side spectral density of the LISA detector noise and the residual foreground of unresolvable galactic binary white dwarfs (Amaro-Seoane et al. 2017; Robson et al. 2019). To keep consistent with the criteria used in Babak et al. (2017), we choose $\rho = 20$ as the threshold of EMRI detections. For EMRIs with $\rho > 20$, we forecast the model parameter constraints with Fisher matrix

$$F_{ij} = \left\langle \frac{\partial h_I}{\partial \lambda_i} \middle| \frac{\partial h_I}{\partial \lambda_j} \right\rangle + \left\langle \frac{\partial h_{II}}{\partial \lambda_i} \middle| \frac{\partial h_{II}}{\partial \lambda_j} \right\rangle, \quad (10)$$

where $\lambda_{i,j}$ ($i, j = 1, \dots, 13$) are the EMRI model parameters briefed in the previous paragraph. The $1\text{-}\sigma$ uncertainty of parameter λ_i is $\sigma(\lambda_i) = \sqrt{C_{ii}}$ with $C_{ij} := F_{ij}^{-1}$ being the covariance matrix.

The volume of the 3D error box is $\delta V = r^3(z) \times \pi \sin \theta_s \sqrt{C_{\theta_s \theta_s} C_{\phi_s \phi_s} - C_{\theta_s \phi_s} C_{\phi_s \theta_s}} \sigma(\ln D_L)$, where $r(z) = \int_0^z \frac{dz'}{H(z')}$ is the comoving distance from the EMRI source to the earth, with $H(z)$ being the Hubble expansion rate. Inside the error box, we expect to see δN_{gal} galaxies, with $\delta N_{\text{gal}} = \bar{n}_{\text{gal}} \delta V$. Here the average number of galaxies per comoving volume is chosen as $\bar{n}_{\text{gal}} = 10^{-2} \text{ Mpc}^{-3}$ (consistent with Kuns et al. 2019). In Fig. 3, we show the δN_{gal} distribution at each redshift, where we find 13% of the detectable EMRIs with $z < 0.5$ can be traced back to their host galaxies, i.e., ~ 8 to ~ 234 EMRIs and their host galaxies can be identified by LISA in the maximum mission duration ≈ 10 years (Amaro-Seoane et al. 2017).

In Fig. 4, we also show the sky resolution $\delta \Omega_s$ and spin direction \hat{a} resolution $\delta \Omega_a$ of detectable EMRIs at each redshift, where $\delta \Omega_s := 2\pi \sin \theta_s \sqrt{C_{\theta_s \theta_s} C_{\phi_s \phi_s} - C_{\theta_s \phi_s} C_{\phi_s \theta_s}}$ and $\delta \Omega_a$ is defined in a similar way. They will be used in estimating the data errorbars of MBH spins and MBH-host galaxy spin direction correlations.

4. BAYESIAN MODEL SELECTION

As explained in the previous two sections, different growth channels will leave different imprints on MBH spins and on MBH-host galaxy spin direction correlations. The former can be measured by LISA from EMRIs, and the latter can be measured by LISA in combination with galaxy spectroscopic surveys. In this section, we will quantitatively explore how likely these channels can be distinguished given data of MBH spins and MBH-host galaxy spin correlations.

According to Bayes theorem, the posterior probability $\mathcal{P}(\lambda|D, \mathbf{m})$ for the parameters λ of a model m given data D is related to the likelihood $\mathcal{P}(D|\lambda, \mathbf{m})$ of seeing data D under model m with model parameter λ by

$$\mathcal{P}(\lambda|D, \mathbf{m}) = \frac{\mathcal{P}(D|\lambda, \mathbf{m})\mathcal{P}(\lambda|\mathbf{m})}{\mathcal{E}(D|\mathbf{m})}, \quad (11)$$

where $\mathcal{P}(\lambda|\mathbf{m})$ is the prior and $\mathcal{E}(D|\mathbf{m}) = \int \mathcal{P}(D|\lambda, \mathbf{m})\mathcal{P}(\lambda|\mathbf{m})d\lambda$ is the evidence of model m given data D . To determine the

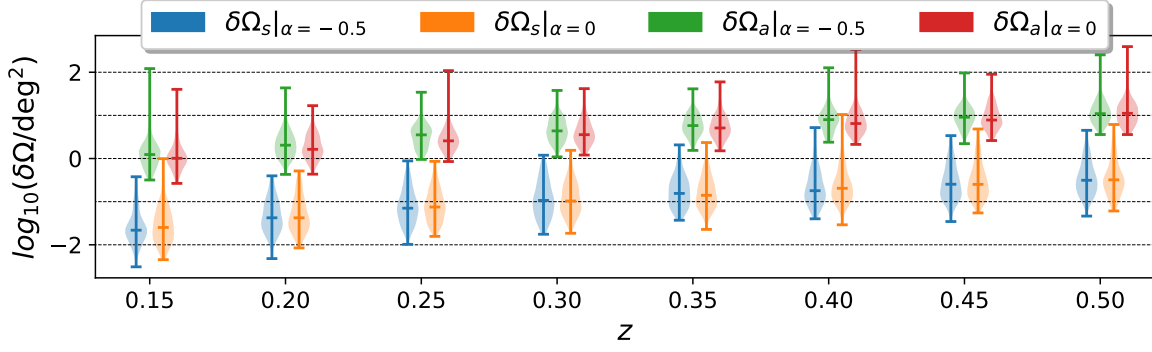


Figure 4. Distributions of sky resolution $\delta\Omega_s$ and spin direction \hat{a} resolution $\delta\Omega_a$ of detectable EMRIs at each redshift z .

(de)preference of models m_1 over m_2 based on data D , we calculate the Bayes factor

$$\mathcal{B}_{m_2}^{m_1}(D) = \frac{\mathcal{E}(D|m_1)}{\mathcal{E}(D|m_2)}. \quad (12)$$

If $\mathcal{B}_{m_2}^{m_1} > 1$, m_1 is a better model than m_2 ; and if $\mathcal{B}_{m_2}^{m_1} < 1$, m_2 is better. According to Jeffreys' evidence scale, $\ln \mathcal{B}_{m_2}^{m_1} > 5$ is interpreted as m_1 is overwhelmingly better than m_2 and equivalently $\ln \mathcal{B}_{m_2}^{m_1} < -5$ as m_2 is overwhelmingly better.

In the context of this work, there is no free parameter in the considered models (Fig. 2), thus the evidence calculation is simplified as $\mathcal{E}(D|m) = \mathcal{P}(D|m)$. In order to calculate the likelihood $\mathcal{P}(D|m)$, we first divide data into N_B bins B_i ($i = 1, \dots, N_B$), and count the number of events in each bin $\{n_i\}$. Each model will predict an average probability of events occurring in each bin $P_i(m) := \int_{B_i} P(d|m) dd$ (see Fig. 2 for the probability distribution functions $P(d|m)$). Events in different bins are independent and the number of events in each bin should satisfy Poisson distribution with an average probability P_i , therefore the likelihood is written as (Gair et al. 2010, 2011)

$$\begin{aligned} \mathcal{P}(D|m) &= \prod_{i=1}^{N_B} \frac{[N_D(m)P_i(m)]^{n_i} e^{-N_D(m)P_i(m)}}{n_i!}, \\ &= [N_D(m)]^{\sum n_i} e^{-N_D(m)} \prod_{i=1}^{N_B} \frac{[P_i(m)]^{n_i}}{n_i!}, \end{aligned} \quad (13)$$

where $N_D(m)$ is the number of events predicted by model m , and $N_D(m)P_i(m)$ is the expected number of events in bin B_i , and we have used the normalization condition $\sum P_i(m) = 1$ in the second equal sign. That is to say, different models predict not only different distributions $P_i(m)$ of data but also different occurrences $N_D(m)$ of data, both of which contribute to model selections. In fact, the total number $N_D(m)$ is commonly more uncertain than the distribution $P_i(m)$. In this paper, we will only use the distribution $P_i(m)$ information to distinguish different channels, i.e., we set $N_D(m)$ to be same

for different models, and we obtain

$$\mathcal{P}(D|m) = \text{const} \times \prod_{i=1}^{N_B} \frac{[P_i(m)]^{n_i}}{n_i!}. \quad (14)$$

In reality, any data point is subject to some measurement uncertainty, $D = \{d^j \pm \delta d^j\}$. We model the true value of event j with a probability distribution $\mathcal{N}(d - d^j, \delta d^j)$ and assign a fractional occurrence $\int_{B_i} \mathcal{N}(d - d^j, \delta d^j) dd$ into each bin B_i . In the continuum limit (small bins limit), Eq. (14) simplifies as

$$\mathcal{P}(D|m) = \text{const} \times \prod_{j=1}^{N_D} P_j(m), \quad (15)$$

where $P_j(m) = \int P(d|m) \mathcal{N}(d - d^j, \delta d^j) dd$.

In our case, data D includes both the MBH spins $D_1 = \{|a^j| \pm \delta a^j\}$ ($j = 1, \dots, N_1$) of the EMRIs detected by LISA and the MBH-host galaxy spin correlations $D_2 = \{\hat{a}_\perp^j \cdot \hat{L}_\perp^j \pm \delta_{aL}^j\}$ ($j = 1, \dots, N_2$), where the error bar δ_{aL}^j is obtained from Fisher forecasts explained in the previous section, while δ_{aL}^j depends on the spin direction uncertainty $\delta\Omega_a$, the sky location uncertainty $\delta\Omega_s$, the angle between the spin direction and the LoS $\theta_{a,LoS}$, and the uncertainty δ_L^j of \hat{L}_\perp^j . As shown in Bundy et al. (2015) and Krolewski et al. (2019), the galaxy spin direction \hat{L}_\perp^j can be measured with uncertainty $\delta_L^j \approx 1^\circ$. From Fig. 4, the sky resolution $\delta\Omega_s$ of LISA turns out to be ~ 30 times better than that of MBH spin direction $\delta\Omega_a$. As a result, we find δ_{aL}^j is dominated by the uncertainty of MBH spin direction $\delta\Omega_a^j$. In terms of azimuthal angles, $\hat{a}_\perp \cdot \hat{L}_\perp \pm \delta_{aL} = \cos^{-1}(\phi_{aL} \pm \delta\phi_{aL})$, we have $\delta\phi_{aL} \approx \sqrt{\frac{\delta\Omega_a}{2\pi}} / \sin^2 \theta_{a,LoS}$, where ϕ_{aL} is the angle between \hat{a}_\perp and \hat{L}_\perp , and $\delta\phi_{aL}$ is its uncertainty.

To illustrate how well different growth channels can be distinguished from each other based on the MBH spin magnitudes data D_1 and MBH-host galaxy spin correlation data D_2 , we take a model m_2 as the true underlying model and generate 256 realizations of D_1 and D_2 sampled from the corresponding distributions shown in Fig. 2 and 3. We conservatively take the data sizes of $N_1 = 60$ and $N_2 = 8$. For

$m_1 \backslash m_2$	WM		CoA	
DM	-195 ± 16	(-210 ± 16)	-267 ± 12	(-283 ± 12)
WM			-10 ± 3.8	(-10 ± 3.8)
CoA	-35 ± 14	(-35 ± 14)		
ChA1	-35 ± 14	(-50 ± 14)	0 ± 0	(-15 ± 2.2)
ChA2	-1.2 ± 1.6	(-16 ± 2.7)	-6.8 ± 3.6	(-22 ± 3.8)

Table 1. Bayes factors $\ln \mathcal{B}_{m_2}^{m_1}$ of model m_1 relative to m_2 , where ChA1 = $\text{ChA}|_{\Delta M/M \approx 4}$ and ChA2 = $\text{ChA}|_{\Delta M/M \approx 1}$. In each column, we take m_2 as the true underlying model and generate data $D_1 = \{|a^j|\}$ ($j = 1, \dots, 60$) and data $D_2 = \{\alpha_1^k \cdot L_1^k\}$ ($k = 1, \dots, 8$). Numbers outside parentheses are the Bayes factors $\ln \mathcal{B}_{m_2}^{m_1}(D_1)$ and numbers inside are $\ln \mathcal{B}_{m_2}^{m_1}(D_1 + D_2)$. We do not include models ChA3 and ChA4 simply because they predict distinct spin distributions that can easily be indentified by eye.

each realization of data, we can calculate the Bayes factors $\mathcal{B}_{m_2}^{m_1}$ of model m_1 relative to m_2 given data D_1 or given both data $D_{1,2}$ using Eqs. (12,15). In Table 1, we list the results of $\ln \mathcal{B}_{m_2}^{m_1}$, with m_2 being Wet Merger or Coherent Accretion, and m_1 being Dry Merger (DM), Wet Merger (WM), Coherent Accretion (CoA) or Chaotic Accretion (ChA). If WM is the true underlying model, we find it can be distinguished from DM/CoA/ChA1 with overwhelming evidence ($|\ln \mathcal{B}_{m_2}^{m_1}| > 5$) at $12/2.1/2.1 \sigma$ confidence level, while is indistinguishable from ChA2 with data D_1 only. Adding data D_2 into consideration, the Bayes factor contrasts $|\ln \mathcal{B}_{m_2}^{m_1}|$ increase by 15 for $m_1 = \text{DM/ChA1/ChA2}$, and WM can be distinguished from DM/CoA/ChA1/ChA2 with overwhelming evidence at $13/2.1/3.2/4.1 \sigma$ confidence level. Similar behaviors are found if the underlying model is CoA.

5. DISCUSSION

Both the formation of BH seeds and the growth history of MBHs leave imprints on the mass function of MBHs, on the distribution of MBH spins and on the MBH-host galaxy spin direction correlations. The mass function can be reconstructed from LISA detected MBH coalescence from high redshift to local universe, the spin distribution can be measured from LISA detected EMRIs and the spin direction correlations can be measured in combination with galaxy spectroscopic surveys. In this paper, we show that different growth channels are partially distinguished from the MBH spins, and can be significantly better distinguished in combination with even a rather conservative number of the spin direction correlation measurements.

In analyzing the spin signatures of different growth channels, we have used rather simplified assumptions. For example, we simply considered two extreme cases in analyzing MBH mergers: wet mergers where gas disks are heavy enough to capture the MBH binaries onto them and therefore enable a tight (remnant) MBH-host galaxy spin direction correlation; dry mergers where there is no gas disk at all

and MBH binary orbits are randomly oriented with respect to the galaxy disks. Even a MBH merger is completely dry (in a gas free environment), there could be a mild (remnant) MBH-host galaxy spin direction correlation, because both spin directions are affected by the orbit direction of the pre-merger galaxy pair. To accurately compute this correlation, one need to keep track of the evolution of MBH pairs driven by all the processes outlined in Sec. 2.2 during multi galaxy mergers. Extracting the meaningful initial conditions for the final inspiral and merger of the inner MBH binary from cosmological N-body simulations is particularly challenging. To our knowledge, no self-consistent study of this problem is available. In a more economical approach, coarse-grain simulation results of galaxy mergers are used as initial conditions of MBH binaries, from which MBH binaries migrate inwards under different driven processes described with simplified prescriptions which however lose track of both the MBH orbit direction in each merger and the remnant BH spin direction in successive mergers (Sayeb et al. 2020). The growth channel Dry Mergers is distinguished from other channels mainly by their different imprints on MBH spin magnitudes (see the 2nd row of Table 1), therefore ignoring the MBH-host galaxy spin direction correlation arising from Dry Mergers does not undermine our conclusion.

In analyzing accretion, we have assumed a Gaussian distribution $\mathcal{N}(1, 0.05)$ of MBH spins driven by coherent accretion. However, the realistic distributions in each channel may be considerably different. The bias or theoretical uncertainty in assessing the model distribution will inevitably affect the results of model selection. It is difficult to nail down all the theoretical uncertainties in this study, as it depends on many details of accretion that are hard to model from first principle: the disk thickness, the magnetic field strength, the configuration of magnetic fields lines and the matter emission properties of the inner disk. More theoretical efforts along this direction are needed, otherwise in the coming epoch of LISA some of our understanding of MBH formation may be limited by the accuracy of modeling given all the astrophysical processes involved, instead of the data uncertainty.

In reality, more than one dominant channels may play important roles, so that the detected data may imply a mixed distribution from various channels. Then the question becomes how to determine the mixing ratios of various channels based on LISA observations and corresponding electromagnetic counterpart measurements. There have been some efforts towards more accurately modeling the MBH growth taking account of mixed channels and detailed astrophysics (see e.g., Barausse 2012; Sesana et al. 2014; Kulier et al. 2015; Zhang et al. 2020; Bhattacharyya & Mangalam 2020; Sayeb et al. 2020). We expect similar discussion can be applied taking the full spin magnitude and MBH spin -galaxy spin correlation into account.

In this paper, we have shown the huge potential of probing the MBH growth via the MBH-galaxy spin direction correlations, in addition to the spin magnitude distribution. As shown by Kuns et al. (2019), host galaxies of stellar-mass binary BH mergers can be identified from combined observations of a deci-hertz GW detector and a ground based detector to redshift $z \approx 0.3$, i.e., ~ 400 pairs of binary BH-host galaxy would be identified per year (assuming a constant merger rate $60 \text{ Gpc}^{-3}\text{yr}^{-1}$). If there is a non-negligible correlation between the orbital angular momentum of field-borne binaries and the rotation direction of their host galaxies, it will be interesting to explore what we can learn from these stellar-mass systems.

ACKNOWLEDGEMENTS

Z.P. and H.Y. are supported by the Natural Sciences and Engineering Research Council of Canada and in part by Perimeter Institute for Theoretical Physics. Research at Perimeter Institute is supported in part by the Government of Canada through the Department of Innovation, Science and Economic Development Canada and by the Province of Ontario through the Ministry of Colleges and Universities.

REFERENCES

- Abel, T., Bryan, G. L., & Norman, M. L. 2002, *Science*, 295, 93
- Amaro-Seoane, P., Audley, H., Babak, S., et al. 2017, arXiv e-prints, arXiv:1702.00786
- Armitage, P. J. 2013, *Astrophysics of Planet Formation*
- Armitage, P. J., & Natarajan, P. 2002, *ApJL*, 567, L9
- Babak, S., Gair, J., Sesana, A., et al. 2017, *PhRvD*, 95, 103012
- Barack, L., & Cutler, C. 2004, *PhRvD*, 69, 082005
- Barausse, E. 2012, *MNRAS*, 423, 2533
- Barausse, E., Bellovary, J., Berti, E., et al. 2015, in *Journal of Physics Conference Series*, Vol. 610, *Journal of Physics Conference Series*, 012001
- Barausse, E., & Rezzolla, L. 2009, *ApJL*, 704, L40
- Bardeen, J. M., & Petterson, J. A. 1975, *ApJL*, 195, L65
- Bardeen, J. M., Press, W. H., & Teukolsky, S. A. 1972, *ApJ*, 178, 347
- Begelman, M. C., Blandford, R. D., & Rees, M. J. 1980, *Nature*, 287, 307
- Begelman, M. C., Volonteri, M., & Rees, M. J. 2006, *MNRAS*, 370, 289
- Berti, E., & Volonteri, M. 2008, *ApJ*, 684, 822
- Bhattacharyya, D., & Mangalam, A. 2020, *ApJ*, 895, 130
- Boco, L., Lapi, A., & Danese, L. 2020, *ApJ*, 891, 94
- Bundy, K., Bershady, M. A., Law, D. R., et al. 2015, *ApJ*, 798, 7
- Chandrasekhar, S. 1943, *ApJ*, 97, 255
- Chua, A. J. K., & Gair, J. R. 2015, *Classical and Quantum Gravity*, 32, 232002
- Chua, A. J. K., Moore, C. J., & Gair, J. R. 2017, *PhRvD*, 96, 044005
- Colpi, M. 2014, *SSRv*, 183, 189
- Colpi, M., Callegari, S., Dotti, M., & Mayer, L. 2009, *Classical and Quantum Gravity*, 26, 094029
- Di Matteo, T., Khandai, N., DeGraf, C., et al. 2012, *ApJL*, 745, L29
- Dotti, M., Colpi, M., & Haardt, F. 2006, *MNRAS*, 367, 103
- Dotti, M., Colpi, M., Haardt, F., & Mayer, L. 2007, *MNRAS*, 379, 956
- Dotti, M., Colpi, M., Pallini, S., Perego, A., & Volonteri, M. 2013, *ApJ*, 762, 68
- Dotti, M., Volonteri, M., Perego, A., et al. 2010, *MNRAS*, 402, 682
- Escala, A., Larson, R. B., Coppi, P. S., & Mardones, D. 2005, *ApJ*, 630, 152
- Ferrarese, L., & Merritt, D. 2000, *ApJL*, 539, L9
- Fragione, G., & Silk, J. 2020, arXiv e-prints, arXiv:2006.01867
- Gair, J. R., Babak, S., Sesana, A., et al. 2017, in *Journal of Physics Conference Series*, Vol. 840, *Journal of Physics Conference Series*, 012021
- Gair, J. R., Sesana, A., Berti, E., & Volonteri, M. 2011, *Classical and Quantum Gravity*, 28, 094018
- Gair, J. R., Tang, C., & Volonteri, M. 2010, *PhRvD*, 81, 104014
- Gammie, C. F., Shapiro, S. L., & McKinney, J. C. 2004, *ApJ*, 602, 312
- Gerosa, D., Rosotti, G., & Barbieri, R. 2020, arXiv e-prints, arXiv:2004.02894
- Haemmerlé, L., Mayer, L., Klessen, R. S., et al. 2020, *SSRv*, 216, 48
- Heger, A., & Woosley, S. E. 2002, *ApJ*, 567, 532
- Hofmann, F., Barausse, E., & Rezzolla, L. 2016, *ApJL*, 825, L19
- Huerta, E. A., & Gair, J. R. 2009, *PhRvD*, 79, 084021
- Hughes, S. A. 2002, *MNRAS*, 331, 805
- Kawaguchi, T. 2003, *ApJ*, 593, 69
- Kawaguchi, T., Aoki, K., Ohta, K., & Collin, S. 2004, *A&A*, 420, L23
- Kawamura, S., Ando, M., Seto, N., et al. 2020, arXiv e-prints, arXiv:2006.13545
- King, A. 2003, *ApJL*, 596, L27
- King, A. R., Lubow, S. H., Ogilvie, G. I., & Pringle, J. E. 2005, *MNRAS*, 363, 49
- King, A. R., & Pringle, J. E. 2006, *MNRAS*, 373, L90
- King, A. R., Pringle, J. E., & Hofmann, J. A. 2008, *MNRAS*, 385, 1621
- Kormendy, J., & Ho, L. C. 2013, *ARA&A*, 51, 511

- Krolewski, A., Ho, S., Chen, Y.-C., et al. 2019, *ApJ*, 876, 52
- Kulier, A., Ostriker, J. P., Natarajan, P., Lackner, C. N., & Cen, R. 2015, *ApJ*, 799, 178
- Kuns, K. A., Yu, H., Chen, Y., & Adhikari, R. X. 2019, arXiv e-prints, arXiv:1908.06004
- Latif, M. A., & Ferrara, A. 2016, *PASA*, 33, e051
- Li, J., & Cao, X. 2019, *ApJ*, 886, 92
- Li, L.-X. 2012, *MNRAS*, 424, 1461
- Lodato, G., & Gerosa, D. 2013, *MNRAS*, 429, L30
- Madau, P., & Rees, M. J. 2001, *ApJL*, 551, L27
- Maggiore, M., Van Den Broeck, C., Bartolo, N., et al. 2020, *JCAP*, 2020, 050
- Maio, U., Dotti, M., Petkova, M., Perego, A., & Volonteri, M. 2013, *ApJ*, 767, 37
- Marconi, A., & Hunt, L. K. 2003, *ApJL*, 589, L21
- Marconi, A., Risaliti, G., Gilli, R., et al. 2004, *MNRAS*, 351, 169
- Mayer, L. 2013, *Classical and Quantum Gravity*, 30, 244008
- Mayer, L., Kazantzidis, S., Escala, A., & Callegari, S. 2010, *Nature*, 466, 1082
- Mayer, L., Kazantzidis, S., Madau, P., et al. 2007, *Science*, 316, 1874
- McConnell, N. J., & Ma, C.-P. 2013, *ApJ*, 764, 184
- McGee, S., Sesana, A., & Vecchio, A. 2020, *Nature Astronomy*, 4, 26
- Mestel, L. 1963, *MNRAS*, 126, 553
- Milosavljević, M., & Merritt, D. 2003, *ApJ*, 596, 860
- Motloch, P., Yu, H.-R., Pen, U.-L., & Xie, Y. 2020, arXiv e-prints, arXiv:2003.04800
- Murray, N., Quataert, E., & Thompson, T. A. 2005, *ApJ*, 618, 569
- Natarajan, P., & Pringle, J. E. 1998, *ApJL*, 506, L97
- Omukai, K. 2001, *ApJ*, 546, 635
- Peng, C. Y. 2007, *ApJ*, 671, 1098
- Rees, M. J. 1984, *ARA&A*, 22, 471
- Robson, T., Cornish, N. J., & Liu, C. 2019, *Classical and Quantum Gravity*, 36, 105011
- Rubbo, L. J., Cornish, N. J., & Poujade, O. 2004, *PhRvD*, 69, 082003
- Sayeb, M., Blecha, L., Kelley, L. Z., et al. 2020, arXiv e-prints, arXiv:2006.06647
- Scheuer, P. A. G., & Feiler, R. 1996, *MNRAS*, 282, 291
- Sesana, A., Barausse, E., Dotti, M., & Rossi, E. M. 2014, *ApJ*, 794, 104
- Sesana, A., Gair, J., Berti, E., & Volonteri, M. 2011, *PhRvD*, 83, 044036
- Sesana, A., Volonteri, M., & Haardt, F. 2009, *Classical and Quantum Gravity*, 26, 094033
- Shakura, N. I., & Sunyaev, R. A. 1973, *A&A*, 500, 33
- Shapiro, S. L. 2005, *ApJ*, 620, 59
- Souza Lima, R., Mayer, L., Capelo, P. R., & Bellovary, J. M. 2017, *ApJ*, 838, 13
- Thorne, K. S. 1974, *ApJ*, 191, 507
- Volonteri, M., Haardt, F., & Madau, P. 2003, *ApJ*, 582, 559
- Volonteri, M., & Rees, M. J. 2005, *ApJ*, 633, 624
- Volonteri, M., Sikora, M., Lasota, J. P., & Merloni, A. 2013, *ApJ*, 775, 94
- Wang, J.-M., Hu, C., Li, Y.-R., et al. 2009, *ApJL*, 697, L141
- Yu, Q. 2002, *MNRAS*, 331, 935
- Zhang, X., & Lu, Y. 2019, *ApJ*, 873, 101
- Zhang, X., Lu, Y., Wang, D., & Fang, T. 2020, *ApJ*, 896, 87